On-demand spatiotemporal programming of collective cell migration via bioelectric stimulation

Tom J. Zajdel[a,1], Gawoon Shim[a,1], Linus Wang[a], Alejandro Rossello-Martinez[a,b], and Daniel J. Cohen[a,*]

[a]Department of Mechanical and Aerospace Engineering, Princeton University, Princeton, NJ 08544, United States
[b]Department of Aeronautics, Imperial College London, London SW7 2AZ, United Kingdom

Directed cell migration is critical across biological processes spanning healing to cancer invasion, yet no tools allow such migration to be interactively guided. We present a new bioreactor that harnesses electrotaxis—directed cell migration along electric field gradients—by integrating multiple independent electrodes under computer control to dynamically program electric field patterns, and hence steer cell migration. Using this platform, we programmed and characterized multiple precise, two-dimensional collective migration maneuvers in renal epithelia and primary skin keratinocyte ensembles. First, we demonstrated on-demand, 90-degree collective turning. Next, we developed a universal electrical stimulation scheme capable of programming arbitrary 2D migration maneuvers such as precise angular turns and directing cells to migrate in a complete circle. Our stimulation scheme proves that cells effectively time-average electric field cues, helping to elucidate the transduction time scales in electrotaxis. Together, this work represents a fundamentally different platform for controlling cell migration with broad utility across fields.

Keywords: directed migration, collective migration, electrotaxis, galvanotaxis, bioelectricity

[1]**These authors contributed equally.**
Correspondence:** ***danielcohen@princeton.edu

Introduction

As directed and large-scale collective cell migration underlie key multicellular processes spanning morphogenesis, healing, and cancer progression, a tool allowing us to shepherd such migration would enable new possibilities across cell biology and biomedical engineering (Friedl and Gilmour, 2009). The key requirements for such a tool are that it should be: (1) broadly applicable across multiple cell and tissue types, and (2) truly interactive to allow spatiotemporal control. Chemotaxis, while an obvious contender, does not broadly apply across cell types as it requires specific ligand-receptor interactions, nor is it easily programmable given the difficulties in interactive, spatiotemporal chemical dosing (Li and Lin, 2011; Berthier and Beebe, 2014; Kress et al., 2009). Micropatterned proteins or surface topographies, in contrast, easily direct cellular motion in many cell types, but these too cannot be dynamically changed to adjust cell migration (Xiong et al., 2019). Finally, while optogenetics can afford truly interactive activation of migratory processes at a subcellular level (Toettcher et al., 2013), such approaches must practically be tailored to single cells and require genetic modification, thereby narrowing applicability and scaling poorly for large systems.

Mounting evidence points to electrochemical cues as the ideal foundation on which to build a general cellular herding system. Beginning with du Bois-Reymond's discovery 175 years ago that skin wounds possess an endogenous electric field (Du Bois-Reymond, 1849), it is now well-established that: (1) 1-10 $\mathrm{V\,cm^{-1}}$ electric fields are natural, emergent responses to ionic imbalances that arise in vivo during morphogenesis, regeneration, and pathogenesis (McCaig et al., 2009; Nuccitelli, 2003); (2) cells transduce DC electrical cues into navigational cues and migrate along the field gradient in a process called 'electrotaxis' or 'galvanotaxis'; and (3) electrotaxis is remarkably widespread across diverse systems including at least 20 diverse mammalian cell types, cellular slime molds, zebrafish, and frogs (Cortese et al., 2014; McCaig et al., 2009). Presently, the electrotactic response is thought to derive from field-induced aggregation of as yet unknown membrane receptors that induce front-rear migratory polarity. Much work has revealed that such endogenous fields likely act on receptors either via electrophoresis (electrostatic force) or electro-osmotic-flow (shear force) rather than directly acting on any intracellular components (Allen et al., 2013), and that these receptors modulate downstream migratory signaling (e.g. via PI3K and PTEN) (Zhao et al., 2006). While elucidation of these mechanisms is an active, ongoing field of study, electrotaxis is undeniably a powerful migratory phenomenon with exciting potential as a tool to manipulate cell migration.

As electric fields can be harnessed to direct cellular migration, modern electronic tools and approaches should enable unprecedented control over tissue dynamics. However, contemporary electrotaxis work focuses on studying electrotaxis as a phenomenon rather than as a tool, and the instrumentation has changed little over the past 100+ years (Dineur, 1891; Song et al., 2007) where only simple, static DC fields with single anode/cathode pairs are used (Tai et al., 2009; Sroka et al., 2018; Tandon et al., 2009; Cohen et al., 2014). Such systems only allow migration to be regulated either forward or backwards along fixed trajectories rather than affording interactive and dynamic control (e.g. optogenetics). Further, the vast majority of electrotaxis studies focus on single cells due to experimental complexities, and the few collective-level electrotaxis studies (Li et al., 2012; Cohen et al., 2014; Lalli and Asthagiri, 2015; Bashirzadeh et al., 2018; Cho et al., 2018) have focused on elucidating biological or biophysical questions rather than advancing the infrastructure or exploring the limits of the phenomenon. We believe that modernized bioelectric interfaces will make the field far more approachable and substantially increase the utility of electrotaxis itself,

PREPRINT

bringing us much closer to being able to deploy electrotaxis as a useful tool to direct cell migration for both fundamental migration research and applied contexts such as expedited healing.

To illustrate the value of electrotaxis as a tool, we present the first instance of freely programmable, two-dimensional herding of collective cell migration using a newly designed, multi-electrode electro-bioreactor which we call SCHEEPDOG: Spatiotemporal Cellular HErding with Electrochemical Potentials to Dynamically Orient Galvanotaxis. Here we describe the design and fabrication of a SCHEEPDOG system, and then validate it by programming large *in vitro* tissues to undergo complex migratory maneuvers such as 90° turns on-command. We next characterize how interactive control with SCHEEPDOG varies in two different tissue types–renal epithelium and primary skin keratinocytes–and explore migration performance metrics to determine how well cells obey given commands. Finally, we present a fully generalized stimulation program relying on independent, orthogonal electrode pairs to generate truly arbitrary, user-designed, dynamic collective migration trajectories, which we demonstrate by programming complex maneuvers into an ensemble of over 10,000 primary skin cells. Together, these findings highlight the surprising plasticity of collective migration, help to elucidate a key detail of how cells might integrate dynamic electrotactic cues, and emphasize the striking fact that electrotaxis may well be the first broadly applicable, arbitrarily programmable cue for directing collective cellular motion in real time.

Results

Design of next-gen electro-bioreactor for multi-axis migration control. Developing electrotaxis into a viable tool for programmatically directing cell migration requires a fundamentally new approach to bioelectric stimulation–interactive, spatiotemporal control of the electric field, and thereby of cell migration. A key limitation of all electrotaxis chamber designs for over 100 years is their use of a single anode/cathode pair to deliver a DC electric field to cells (Dineur, 1891; Song et al., 2007). This intrinsically constrains the ability to direct migration to a single axis of motion, heavily limiting the types of experiments and questions that can be explored. By contrast, the SCHEEPDOG platform is unique as it possesses 4 electrodes under continuous computer control to allow for true spatiotemporal programming of the electric field geometry in 2D (Figure 1). To maximize value and accessibility of SCHEEPDOG, we identified and integrated best-practice design approaches from across the field, and further ensured that the fabrication approach requires only benchtop rapid-prototyping (e.g. no cleanroom) to allow for quick iteration, easy sharing of designs, and reproducibility across laboratories.

SCHEEPDOG is essentially an instrumented, bioelectric flow chamber that incorporates three key design modules: (1) bioreactor architecture; (2) life support; and (3) dynamically programmable electric field generation. The bioreactor housing comprising the culture substrate, cells, and layer-based microfluidic assembly integrates best-practices improving on our prior work and that of others (Cohen et al., 2014; Cho et al., 2018; Sun, 2017) while allowing rapid, flexible assembly of the device components *in situ* around either single cells or pre-engineered tissues (Figures 1a-c,S1). Briefly, cells or tissues are patterned on a substrate using a silicone seeding stencil to define the tissue shape, and then a separate silicone stencil is sandwiched between a laser-cut insert and the cell culture substrate to define a stimulation zone (Figure 1d). Confining cells to a narrow stimulation zone is key to concentrating DC electric fields and maximizing device efficiency (Cohen et al., 2014). Further, such *in situ* assembly around pre-cultured tissues affords both complete control of cell and tissue geometry and composition, as well compatibility with arbitrary culture substrates (which we tested with large glass coverslips in addition to tissue culture Petri dishes).

To accommodate metabolic needs and prevent detrimental electrochemical effects on migrating cells, we integrated a number of new life-support and safeguard systems into SCHEEPDOG. Virtually all DC electrotaxis systems inject Faradaic current across the cells through an anode and a cathode, typically comprised of silver chloride or noble metals, immersed in saline reservoirs (Song et al., 2007). SCHEEPDOG used two pairs of Ag/AgCl electrode foils in saline reservoirs organized along two orthogonal axes, each independently connected to a dedicated computer-controlled current source to compensate for typical electrochemical variations during stimulation. Further, the silver foil electrodes were chloridized electrochemically (Methods, Huang et al. 2013; Vulto et al. 2009) to improve electrode longevity over traditional bleach-based methods. Since cytotoxic electrochemical byproducts are produced at each electrode-electrolyte interface, most electrotaxis systems integrate a salt-bridge diffusion barrier to these byproducts (Schopf et al., 2016), while some use continuous media perfusion across the cells to minimize their concentration (Cole and Gagnon, 2019). SCHEEPDOG integrated both structured agarose bridges (Hou et al., 2014; Huang et al., 2013; Song et al., 2013; Wu et al., 2015) and continuous culture media perfusion to keep tissues oxygenated and free of any electrochemical byproducts (Methods). Together, we attribute these measures to SCHEEPDOG's uncommonly long, stable run-times (8-12 h at least) without any detectable cytotoxicity despite high driving current.

Finally, and critically, the key to SCHEEPDOG is interactive, spatiotemporal control of the electric field, enabled here by using 4 stimulation electrodes grouped into orthogonal pairs (e.g. X and Y axes). Because incorporating two anode-cathode pairs required a large and broad stimulation region, special care was taken to ensure field uniformity within a large stimulation zone to improve throughput (Tsai et al., 2016; Huang et al., 2001; Cohen et al., 2014). To minimize potential field distortion, we designed the integrated agarose bridges to occupy nearly the entire perimeter of the stimulation chamber and to be relatively thin to minimize current leak through unused electrodes (such performance is not possible using prior, single-layer electrotaxis chambers; Figure S2 shows a naive 4-electrode design with non-uniformities). Numeric

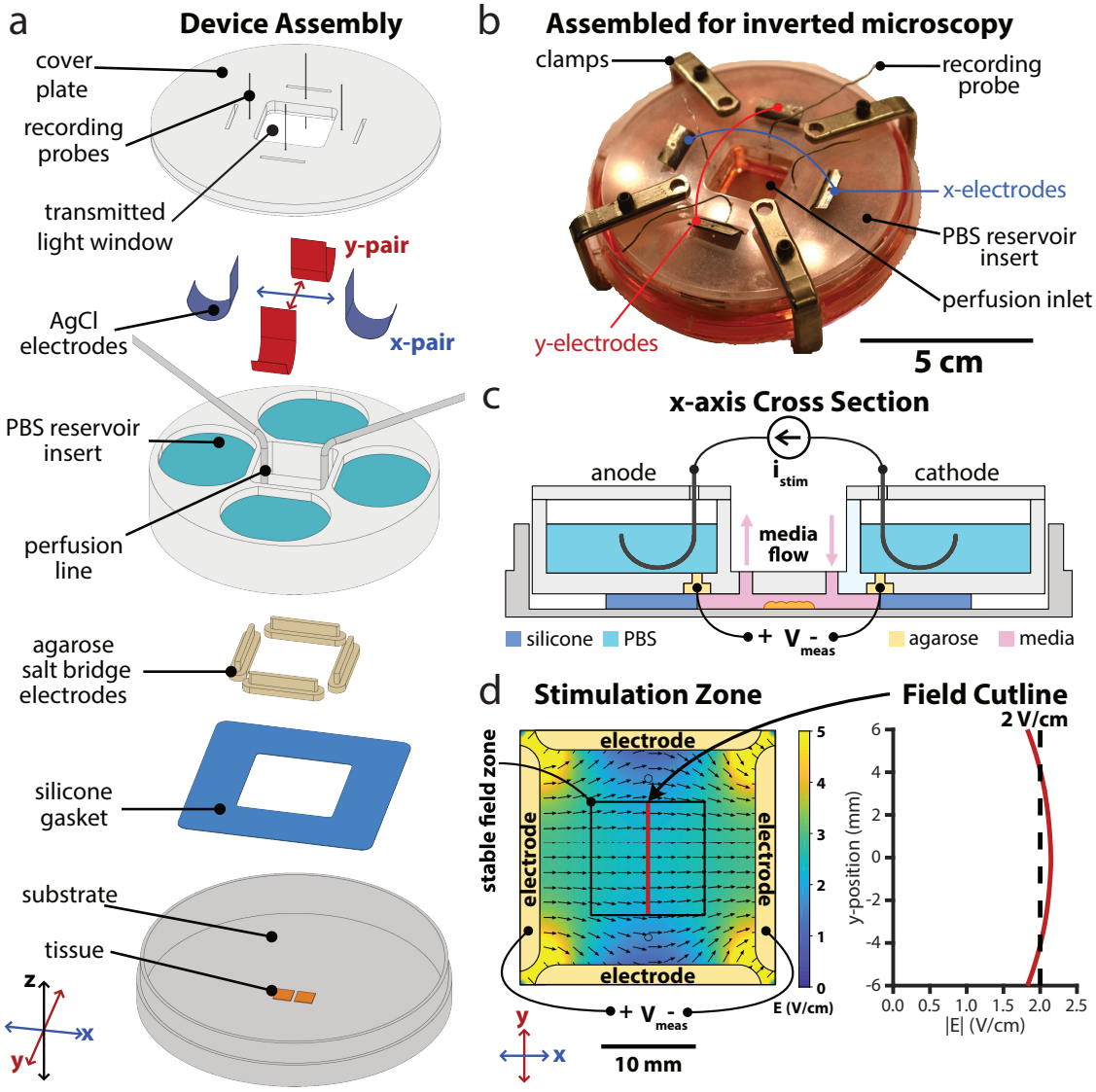

Figure 1. Design of next-gen electro-bioreactor for multi-axis migration control; SCHEEPDOG: Spatiotemporal Cellular HErding with Electrochemical Potentials to Dynamically Orient Galvanotaxis, a bioreactor for two-dimensional, bioelectric control over collective migration. (a) Assembly of the SCHEEPDOG bioreactor within a Petri dish. A silicone stencil defines a stimulation zone in the center of the dish, and tissues are patterned within this region. Four agarose bridges held inside a laser-cut PBS reservoir insert are then pressed against the stencil to fully enclose the stimulation zone. Ag/AgCl electrodes and perfusion lines are added, then a lid is clamped to the assembly and recording probes are inserted into each agarose bridge electrode. (b) Photograph of a fully assembled device. (c) Sectional schematic of one axis of SCHEEPDOG. Each axis features one anode/cathode pair connected to a computer-controlled current supply which provides i_{stim}. A digital oscilloscope records channel voltage V_{meas} to enable closed-loop control. (d) Numeric simulation of the field generated by the device when the horizontal electrode pair is stimulated, showing a stable field zone in the center of the device. See also Figures S1,S2.

simulation of the field was completed in COMSOL (Figure 1d) to determine how the field strength varied when a target strength of 2 V cm^{-1} was applied to the chamber. To ensure uniform stimulation, tissues were kept within a 12x12 mm square region in the center of the SCHEEPDOG platform where field uniformity varied by only $\pm 7\%$ across the culture zone. Additionally, SCHEEPDOG used closed-loop feedback to ensure a temporally stable field (Figure 1c) and monitored the channel voltage with a pair of probing electrodes. Such precision control allowed us to freely program complex stimulation patterns while maintaining constant stimulation strength and field uniformity (Methods).

Validating 2-axis control of collective cell migration. We selected a 90° turn as an archetypal complex maneuver to validate bi-axial, programmable control over directed cell migration. Here, we selected the MDCK epithelium as our initial model system as it is a standard model both for studying large-scale, collective cell migration and for collective electrotaxis in 1D (Cohen et al., 2014; Bashirzadeh et al., 2018; Li et al., 2012). We patterned 5x5 mm MDCK monolayers into SCHEEPDOG, then used automated phase-contrast microscopy to capture 1 h of control data (field OFF) before stimulating at ~2 V cm^{-1} for 2 h along the X-axis ('right') followed by 2 h along the Y-axis ('up'). To better characterize the individual cell trajectories, we tracked ~10,000 single cells within the tissue center and overlaid these trajectories to capture the spread of individual cell responses (Figure 2a,b). The trajectories show that while there is cell-to-cell variation, the

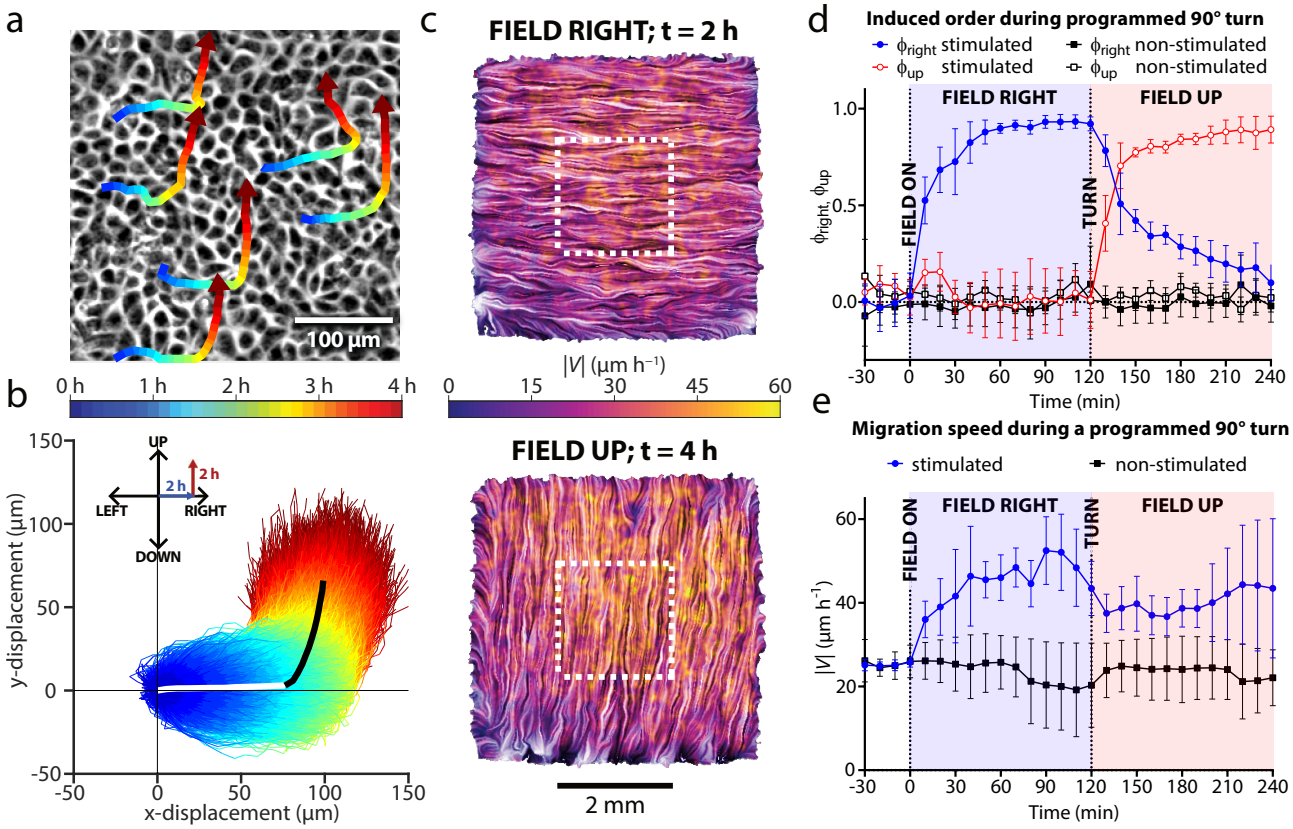

Figure 2. Validating 2-axis control of collective cell migration with a demonstration of collective 90° turns in MDCK cell sheets (trajectories measured from n = 8 tissues). (a) Phase-contrast microscopy image of MDCK tissue stimulated for 2 h 'right', and then 2 h 'up' with overlaid individual cell trajectories with temporal color-coding. (b) Overlaid trajectories of 10,000+ cells. For visual clarity, trajectories within two standard deviations of the mean trajectory (bold white and black overlaid lines indicating the two phases of the turn) are selected and plotted with temporal color-coding (n = 10735 trajectories selected from 11300). Individual trajectories were taken from 2x2 mm central segments of 5x5 mm tissues during induced migration. For visual clarity here, trajectories within two standard deviations of the mean cell trajectory of the data) are selected and plotted with temporal color-coding (n = 10735 trajectories selected from 11300). (c) LIC analysis of an entire MDCK tissue during a programmed 90° turn. The heat map shows the velocity magnitude $|V|$ (µm h^{-1}). White dotted box denotes the 2x2 mm window used for trajectory and PIV analysis. (d) Mean directional order parameter both in the horizontal (blue) and vertical (red) axis during a turn. Data are plotted in 10 min intervals and represent the PIV-derived order averaged across tissues (n = 8). Error bars represent standard deviation across tissues. Dashed vertical lines denote when the field was switched on or changed direction. (e) Mean velocity in the analysis region. Error bars represent the standard deviation across tissues.

population clearly followed an L-shaped trajectory. The cells displaced first by ~75 µm in the X-direction and ~3 µm in the Y-direction during the 'rightward' stimulation period, and then by ~20 µm in the X-direction and ~65 µm in the Y-direction during the 'upward' stimulation period. The small standard deviation of ~15 µm during these maneuvers is equivalent to about ~1 cell body length of fluctuation, showing a relatively high resolution interpretation of the programmed maneuver.

To quantify ensemble-level dynamics during the programmed turn, we next analyzed the overall migratory patterns induced in the tissue using standard tools from swarm dynamics and collective cell migration (Poujade et al., 2007; Cohen et al., 2014). Here, we used particle image velocimetry (PIV) to generate cell migration vector flow fields across the tissues at each time point. From these data, we used Line Integral Convolution (LIC, Thielicke and Stamhuis 2014) visualization to characterize overall migration patterns (streamlines and speeds) during each phase of the turning maneuver (Figure 2c). This approach reveals both the strong horizontal migration during the 'rightward' phase and vertical migration during the 'upward' phase. Additionally, we noted the strongest tissue response within the bulk of the tissue rather than at the edges, which we hypothesize to be due to a combination of contractile differences at the bulk and edge of the tissue (Cho et al., 2018; Trepat et al., 2009), and the fact that MDCK edge cells have been shown to respond differently to electrotactic cues (Cohen et al., 2014). Informed by the static LIC data, we next used the PIV vector field to quantify migratory dynamics over time within the central zone of the tissues (see Methods). Here, we analyzed both ensemble migration speed and directionality order parameters. The directionality order parameter is a measure of coordination in group motion and provides a baseline sense of how well a population responds to a given command (e.g. 'go right'). It is calculated by averaging the cosine of every vector in the PIV vector field with respect to the horizontal axis as shown in Equations 1 and 2:

$$\phi_{right} = \frac{1}{n}\sum_i \cos\theta_i \quad \textbf{(1)}$$

$$\phi_{up} = \frac{1}{n}\sum_i \sin\theta_i \quad \textbf{(2)}$$

ϕ_{right} is extent of motion along the X-axis and ϕ_{up} is the extent of motion along the Y-axis, and both range from -1

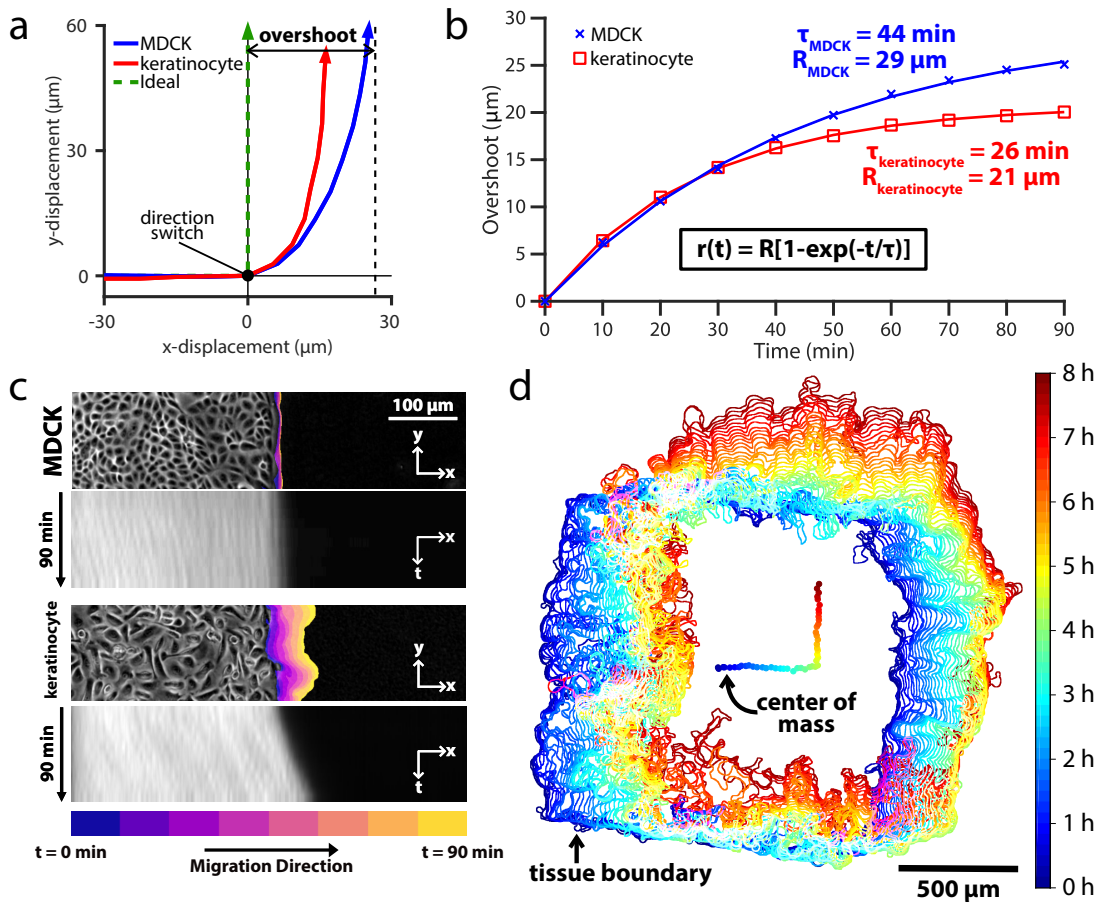

Figure 3. Defining electrotactic peformance metrics. We compared MDCK and keratinocyte tissue electrotaxis during programmed 90° turns. The electric field was directed 'right' for 1.5 h, then 'up' for 1.5 h. Data were analyzed from the 2x2 mm central segments of 5x5 mm tissues. (a) Visualization of the mean trajectory overshoot from the ideal trajectory (green) of the MDCK (blue) and keratinocyte (red) tissues. Trajectories averaged across n = 2 tissues for each cell type (2838 MDCK trajectories and 877 keratinocyte trajectories). (b) Comparison of the overshoot, response time, relaxation time and turn time. Data plotted are the same as from panel (a), with least-squares fit lines overlaid. (c) Boundary displacement and kymographs for MDCK and keratinocyte tissues during the 90 min stimulation to the right. Boundary displacement plots visually indicate extent of outgrowth while the kymographs depict the average edge outgrowth across the entire leading edge of representative tissues. (d) Boundary displacement and tracking of the ensemble center of mass for an 8 h run, with 4 h stimulation in the 'right' and 4 h 'up'. See also Movies S1,S2,S3.

(anti-correlated motion) to 1 (perfect alignment with the commanded direction). Figure 2d plots ϕ_{right} and ϕ_{up} throughout the programmed 90° turn. While ϕ_{right} increases immediately after the field is turned on, there is a ~45 min delay to reach steady-state order (ϕ_{right}~0.9), which reflects the control effort needed to overcome the initially isotropic migration (zero net order) and transition to anisotropic migration (Figure 2a). A similar lag in the increase of ϕ_{up}, or the reorientation time, occurs when the field changes direction from 'right' to 'up'. Here, it is notable that ϕ_{right}–rightward motion–is relatively high for at least 60 min after the command changes from 'right' to 'up'. This persistent rightward motion indicates hysteresis and a mechanical memory in the tissue, likely reflecting strong cell-cell interactions within the monolayer, which may provide initial resistance to re-orientation.

A further sense of the migratory consequences of a programmed maneuver can be seen in the overall change in ensemble speed (Figure 2e) and behavior during the turning transition. Under initial 'rightward' stimulation, migration speed increases from the baseline speed of 25 µm h^{-1} to 50 µm h^{-1} prior to the turn, reaching peak speed 1.5 h into stimulation. Such speed increases during electrotaxis have been previously reported and are hypothesized to derive from more streamlined motion and asymmetric alterations in migratory traction forces (Cohen et al., 2014; Cho et al., 2018). Given that, the transient drop in migration speed during the 'rightward' to 'upward' transition period appears to reflect the initial 'rightward' migration conflicting with a new command for cells to move 'upward.' As cells gradually entrained to the new command, speed increased once again. Further, and despite the transient drop in speed, at no point during the turning maneuver did tissues slow back to baseline speed. These modulations in overall speed during the maneuver suggest that ensemble interactions lead to complex reorientation dynamics that warrant further study. These experiments validate both that SCHEEPDOG can deliver independent X- and Y-axis commands to tissues and that cells can respond to dynamic, orthogonal migration cues, in turn highlighting the surprising plasticity of large scale collective migration.

Defining electrotactic peformance metrics. Having validated programmable electrotactic maneuvers are possible, we next investigated how effectively cells obey programmed

commands, and we determined the practical control parameters and limitations of electrotactic control. To compare electrotactic control in different cell types and in a more physiologically relevant model system, we also tested primary skin keratinocytes collected from neonatal mice and cultured in basal epidermal growth media (Shrestha et al., 2015). To assess relative electrotactic sensitivity, we executed identical 90° turning maneuvers in MDCK and keratinocyte monolayers (5x5 mm tissues, 1 h control period, 90 min of stimulation 'right' and 'up', respectively, ~2 V cm^{-1} field; Movies S1,S2). We assessed performance by measuring the offset error between the mean population trajectory and the ideal trajectory that the cells would have tracked had they responded instantaneously to the field direction switch with no hysteretic effects (perfect turning). The offset error for a stably 'rightward' migrating tissue that is then ordered to migrate 'upward' can be seen in Fig 3a. Here, we compare the mean trajectory of individual trajectories taken from a 2x2 mm central segment to the ideal trajectory. To quantify this difference, we fit the overshoot of each cell type's mean trajectory for 90 min after the stimulation direction changed to a simple first-order response, defined in Equation 3:

$$r(t) = R[1 - \exp(-t/\tau)] \quad \textbf{(3)}$$

where $r(t)$ is the overshoot (µm) at time t (min), R is the final asymptotic overshoot (µm), and τ is the time constant of reorientation (min). Figure 3b shows these fits for both MDCK cells and keratinocytes. This metric demonstrates that MDCKs require nearly ~70% more time than keratinocytes to reorient during a 90° turn (44 min vs 26 min, respectively). Furthermore, the steady state overshoot of keratinocytes is ~20 µm, which is ~30% less than the ~30 µm overshoot for MDCKs. From a control perspective, this indicates that keratinocytes both respond more quickly and turn more tightly than do MDCK cells. We hypothesize that this difference may reflect underlying differences in tissue mechanics (e.g. cell-cell and cell-substrate adhesions) and possible signal transduction differences deserving of further study.

Programming large-scale tissue translation. An exciting aspect of programming directed cell migration is the potential to herd, or physically translate, a tissue or cause it grow in a biased manner. This capability has important implications spanning collective migration research, tissue engineering, and wound healing applications, and is simply not possible with contemporary tools. To evaluate boundary outgrowth, we tracked the leading edges of MDCK and keratinocyte monolayers undergoing electrotaxis. Strikingly, keratinocytes exhibited dramatic outgrowth in the stimulation direction, while MDCKs underwent little to no outgrowth (despite strong internal migration) as shown in Figure 3c when tissues were stimulated for 90 min. The colorized plots and the kymographs indicate that MDCK monolayer edges translated less than 5 µm in the stimulation direction, while keratinocyte monolayer edges translated nearly 75 µm over the same period. Again, it is likely that differences between the cell-types (e.g. adhesions, force transmission) result in different migratory mechanics that explain these behaviors.

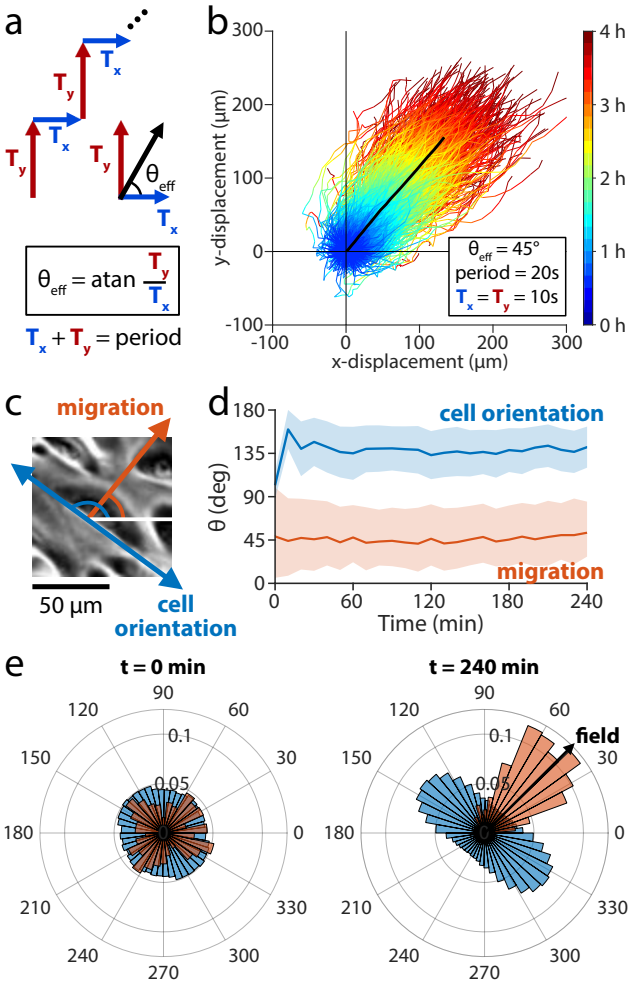

Figure 4. Developing a universal migration control scheme based on rapid switching of electric field directions to enable arbitrary field angles. (a) The stimulation sequence divides a 20 sec stimulation window into two periods: horizontal stimulation (T_x) and vertical stimulation (T_y). The ratio of T_y to T_x determines the effective stimulation angle that the cells experience. (b) Trajectories of 2x2 mm central segments from keratinocyte ensembles across 4 h of stimulation with $\theta_{\text{eff}} = 45°$ (n = 2 ensembles). The mean trajectory is plotted as a thick black line. Tracks within two standard deviations of the mean cell trajectory are selected and plotted as time-coded multicolor lines (n = 900 trajectories selected from 930). (c) Phase contrast image of keratinocyte cell migrating at 45° (red arrow), showing the cell body oriented along 135° (blue arrow). (d) Dominant orientation angle during the 4 h stimulation period as computed by Fourier components analysis, showing a rapid orientation to 135° that persists throughout. Shaded bar is standard deviation in orientation across one representative ensemble. (e) Cell body orientation (blue) and migration direction (red) histograms for a representative tissue at t = 0 min, just as stimulation began, and at t = 240 min, just as stimulation ended. Cell body orientation ranges from 0° to 180° and its distribution is duplicated across the horizontal for visualization purposes. The cells across the ensemble oriented perpendicularly to the migration direction of 45°. See also Movies S4,S5.

We then demonstrated macro-scale programmed translation by commanding a small keratinocyte square (1.4x1.4 mm) to undergo an 8 h turning maneuver with 4 h of stimulation 'rightward' and 'upward', respectively (Movie S3). Images were collected using both phase contrast and Hoechst live nuclear imaging to enable nuclear tracking. Figure 3d presents both the projected tissue boundary over time along with the trajectory of the tissue centroid which clearly traces out a sharp 90° turn with tissue translation of up to 500 µm in each direction. Although the ensemble largely translated across large distances, ~10-15% of the total population appeared to lag behind (Movie S3), indicating likely heterogeneity in electrotactic sensitivity across the population, possibly due to cells at the trailing edge being left behind due to difference in cell-cell contacts. Together, the boundary and bulk displacement data indicate that MDCK cells undergo behavior akin to supracellular migration, perhaps due to more pronounced cell-cell adhesions and differences in cell-substrate interactions leading to different domains of electrotaxis (e.g. edge vs. bulk) (Cohen et al., 2014; Cho et al., 2018; Shellard et al., 2018), while electrotaxing keratinocyte ensembles migrate more akin to 'marching in formation', exhibiting much tighter responses and behaving largely as a unit.

Developing a universal migration control scheme based on the electrotactic timescale. A truly programmable migration controller ought to allow an arbitrary 2D maneuver to be completed by a tissue. To translate this into practice for our 4-electrode design, we hypothesized that a given maneuver could be represented as a serialized sequence of independent X- or Y-axis migration command pulses, akin to an 'etch-a-sketch'. In this control scheme, we deliberately fixed the field strength at ~2 V cm^{-1}, and then altered only the relative duration of X-axis commands versus Y-axis commands, as shown in Figure 4a. We hypothesized that switching back and forth between X- and Y-field directions quickly enough would induce cells to stimulate along the effective, time-averaged field direction along the angle calculated in Figure 4a.

To test this control scheme, we implemented a command sequence to generate a diagonal line at a 45° angle during keratinocyte migration. Here, stimulation time was switched between the X-axis (period T_x) and the Y-axis (period T_y) over repeating 20 sec periods. A $\frac{T_y}{T_x}$ ratio of 1 was used, meaning that each direction was alternately stimulated for 10 sec, 50% of the period, so that the time-averaged electric field would be at a 45° angle with the horizontal (Figure 4a,b, Movie S4). Over a total duration of 4 h, the monolayer displaced 135 µm in the horizontal direction and 155 µm in the vertical, tracking a 49° angle overall (Movie S5). The small deviation from the target angle likely reflects slight misalignment of the camera with respect to the field axes. Notably, individual cell bodies aligned orthogonal to the effective electric field vector, resulting in cell bodies stably orienting at 135° without major fluctuations over time (Figure 4c-e). Such orthogonal alignment between the long axis of a cell and the direction of electrotactic migration is consistent with prior observations in 1D systems (Hammerick et al., 2010; Cho et al., 2018).

That cells appeared to migrate smoothly along this 45° trajectory despite only being stimulated 'right' or 'up' in quick succession appears to confirm the hypothesis that cells effectively time-average the electrotactic commands and therefore perceive a virtual command direction. To validate the generality of both the directional control scheme and compatibility in a different cell type, MDCK cells were programmed to migrate at 60° angles (Figure S3, Movie S6). Together, these data imply that the field-sensing mechanism of electrotaxis must operate on a timescale far faster than the migration response, which occurs on the order of minutes.

Herding cells in a closed circle to demonstrate general, continuous control. To explore the capabilities and limits of control offered by this platform, we programmed a more complex maneuver into a keratinocyte monolayer–a closed circle, which requires continuously adjusted stimulation commands. By modulating the ratio $\frac{T_y}{T_x}$ over time, we discretized the circular path into 80 serial turns of approximately 4.5° equally spaced over an 8 h period as shown in (Figure 5a).

Remarkably, cells successfully tracked this continuously shifting electric field, completing a circular maneuver with an average perimeter of over 300 µm (Figure 5b and Movie S7). To better quantify the population dynamics during this maneuver, we generated angular histograms of migrating tissues at key time-points throughout the 8 h period (Figure 5c). While these show consistent tracking of the command vectors (effective field direction), the persistent lag between the command vector and the direction of average cell migration is also apparent. This angular phase lag averages 25° over the maneuver (Figure 5d) and never catches up to the command vector, suggesting intrinsic limitations to the types and timescales of programmable electrotactic maneuvers at the population level. PIV analysis of velocity (Figure 5e) shows that both v_x and v_y varied sinusoidally and ~90° out of phase with each other, characteristics expected of circular motion. Altogether, these data validate that truly arbitrary programming of cellular maneuvers is possible by discretizing complex maneuvers, and represent the first example to our knowledge of a tissue obeying a prescribed, continuously varying 2D migrational cue.

Discussion

SCHEEPDOG represents a fundamentally new type of electrotaxis platform designed specifically to enable programmable, dynamic control over directed cell migration. Despite the critical importance of such migration across myriad biological processes, no contemporary technology offers such control. Further, electrotaxis platforms have been limited to fixed electric field orientations, nearly exclusively applied to single cells, and used specifically to study electrotaxis itself. While such work is critical, we sought to expand the role of electrotaxis from 'phenomenon' to 'tool'. The result is a fundamentally new platform that can not only advance the study of electrotaxis, but also literally herd cells en masse and on command.

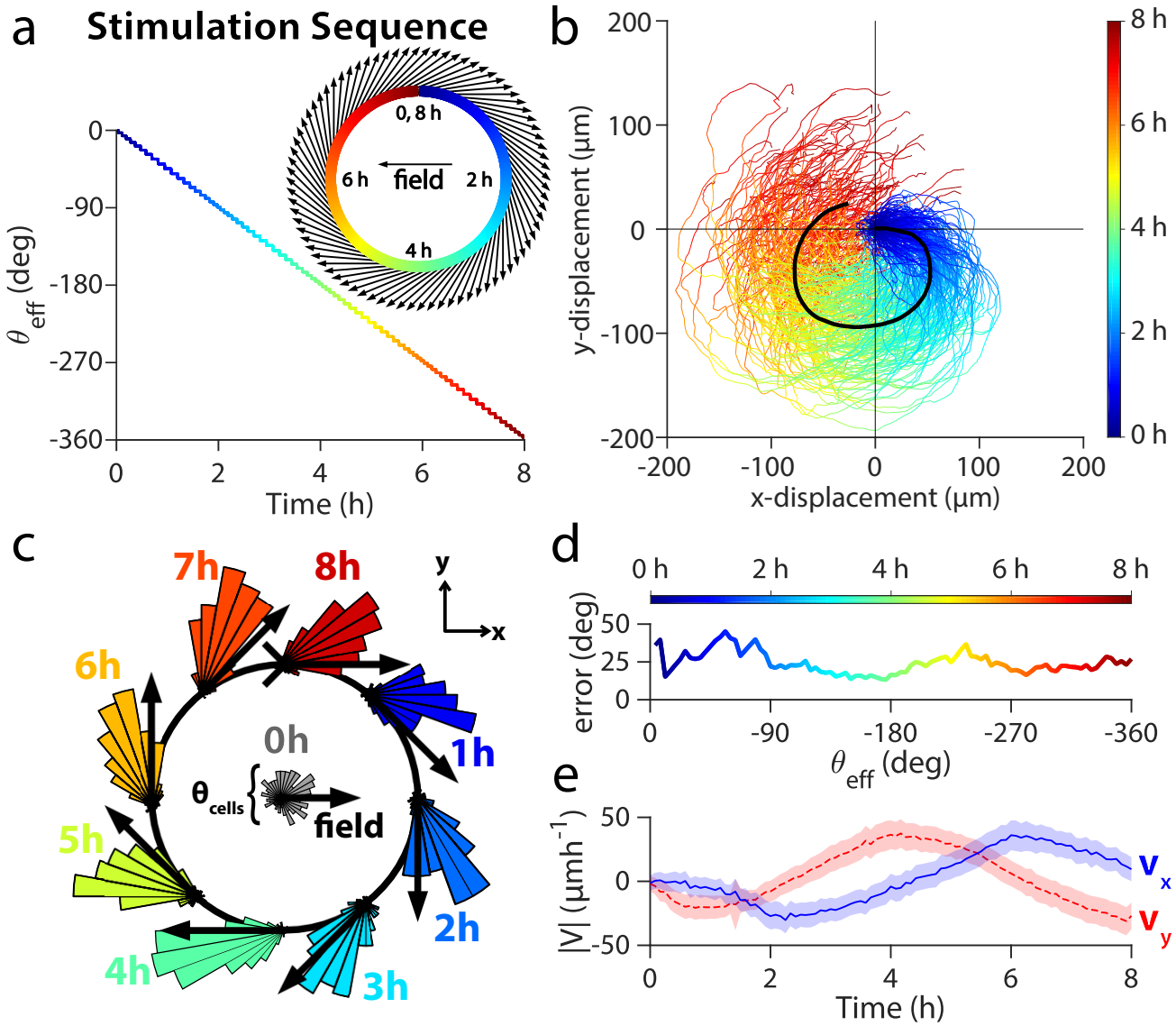

Figure 5. Herding cells in a closed circle to demonstrate general, continuous control. (a) The stimulation sequence used for discretization of the circular maneuver with respect to time. θ_{eff} angle across time for the entire circle is plotted as a multicolor line, while the discretization is overlaid as a black line. Insets show a close up of the first hour of θ_{eff} over time (upper right) and the effective field vectors of stimulation for this period (lower left). (b) Trajectories of 2x2 mm central segments from two keratinocyte tissues throughout 8 h circular stimulation (n = 224 trajectories). (c) Angular histogram of cell velocities calculated from PIV. Black arrows indicate the direction of stimulation. (d) Phase lag between the mean cell migration direction and the effective stimulation direction θ_{eff}. (e) PIV-derived velocity averaged across two tissues in X- (blue) and Y-directions (blue). Shaded region represents standard deviation. See also Movie S7.

We developed SCHEEPDOG to address these limitations and allow for programming of cell migration, taking care to ensure SCHEEPDOG can be manufactured simply and directly integrated in a conventional inverted time-lapse imaging microscope. By integrating 4 independent electrodes under computer control with a layer-based microfluidic assembly design, we created a platform that generates a uniform and symmetric field across tissues and sustains stable long-term culture during electrical stimulation. Using SCHEEPDOG, we programmed truly arbitrary maneuvers ranging from straight diagonal lines to a full circle using only two electrode pairs (Figure 4,5), dynamically switching between them to incrementally 'herd' cells along complicated 2D curves from primitive commands. As numerous studies have shown that the vast majority of tested mammalian cell types undergo electrotaxis, SCHEEPDOG is likely to be valuable across an exceptionally broad range of cell types and applications (Figure 3) (Cortese et al., 2014; McCaig et al., 2009).

Notably, dynamic programming of electrotaxis also provides insights into the key timescales involved. Specifically, our results support the hypothesis that there are two key timescales governing electrotaxis: (1) rapid sensing of the electric field (<10 sec), and (2) slower cellular polarization and migrational response (30 sec to minutes). This separation of scales also occurs in chemotaxis, which has been shown to share certain overlapping signaling and migration infrastructure with electrotaxis (Gao et al., 2015). Our data in Figure 4 that show keratinocytes moving diagonally at 45° in response to rapid and symmetrically alternating X- and Y-direction stimulation (i.e. every 10 sec) suggest that the cells responded

to a time-averaged field direction. The smooth realignment of cell bodies perpendicular to this axis of translation further supports our hypothesis that keratinocytes sensed a composite field from these stimulae. If cells had perceived the stimulation as two distinct cues, there should instead have been a discernible 'wobble' to the long-axis alignment rather than the tight distribution we observed (Figure 4d). The frequency of switching used, 0.33 Hz, led to a single steady-state response, implying that this signal was time-averaged by a slower process in electrotaxis' signal transduction pathway operating on a longer timescale.

To place this behavior in context, consider that the dominant hypothesis in electrotaxis is that DC field stimulation induces the asymmetric distribution of membrane-bound receptors, in turn leading to front-rear polarization. Prior studies on model receptors indicate that full receptor aggregation occurs on the order of 5 minutes during stimulation at physiological field strengths (1-5 V cm^{-1}) (Allen et al., 2013; Sarkar et al., 2019). Given that we can make a cell track a 45° angle by repeatedly cycling the stimulation direction between 'right' and 'up' for 10 seconds in each direction, it is unlikely that affected receptors would have time to fully polarize during any given 10 sec period. Instead, this suggests that the time-averaging behavior we observe likely stems from gradual and increasing polarization of affected receptors throughout our 'right'/'up' cycling, which we hypothesize would cause any affected receptors to gradually aggregate along the time-averaged axis, in turn triggering front rear polarity. This type of malleable receptor aggregation would be compatible with numerous accounts implicating PI3K, PTEN, and PIP2/3 in the electrotaxis transduction process (Meng et al., 2011; Zhao et al., 2006). Future work could employ SCHEEPDOG's dynamic switching capabilites to investigate not only the localization time of common polarity factors, but also the spatiotemporal dynamics of induced cytoskeletal reorganzation, thereby furthering our understanding of how the electrical signal is transduced to establish cell polarity and directed motion–still largely unresolved and an exciting area of research.

Together, electrotaxis as a phenomenon and SCHEEPDOG as a platform address the lack of existing tools to program and steer cell migration en masse, while ensuring broader applicability and more dynamic control than alternative '-taxis' platforms (Fuller et al., 2010). Overcoming the limits of the 1D stimulation scheme that has been the standard for over 100 years (Dineur, 1891; Song et al., 2007), the two-dimensional nature of SCHEEPDOG affords an unprecedented level of control over cell migration, essentially providing 'on-demand' cell migration. This capability offers new possibilities not only for electrotaxis research in its own right, but also for the broader space of cell migration and tissue engineering research. For instance, the ability to precisely modify cell migration in real time means that unique perturbations can be programmed and tailored for specific assays (e.g. studying cytoskeletal re-arrangement during electrotaxis throughout a 'right turn'). Modifying maneuver geometry and timescales can be key to isolating signaling, transcription, and mechanical processes during directed migration. Further, we foresee this form of interactive cell migration control underlying the development of a variety of 'bioelectric band-aids' that might guide and accelerate wound healing, angiogenesis, and other morphogenic processes that rely on endogenous DC electric fields (Barker et al., 1982; Borgens et al., 1977; Zhao et al., 2004). Ultimately, we hope that SCHEEPDOG will help to standardize and refine both design practices and applications of electrotaxis across research fields, promoting accessibility and reproducibility, and better allowing us to harness this unique and powerful bioelectric sheepdog.

Methods

Cell culture. Wild-type MDCK-II cells (courtesy of the Nelson Laboratory, Stanford University) were cultured in Dulbecco's Modified Eagle's Medium with 1 g L^{-1} glucose, 1 g L^{-1} sodium bicarbonate, 10% fetal bovine serum, and 1% penicillin–streptomycin. Primary keratinocytes were harvested from mice (courtesy of the Devenport Laboratory, Princeton University) and cultured in E-medium supplemented with 15% serum and 50 µM calcium. All cells were maintained at 37 °C under 5% CO_2 and 95% relative humidity. Cells were split before 70% confluence and passage number was kept below 20 for MDCKs and 30 for keratinocytes for all experiments.

Device fabrication and assembly. SCHEEPDOG was designed for simultaneous fluid perfusion and electrical stimulation. The chamber geometry was designed in CAD software (Autodesk Fusion) and then simulated in finite element software (COMSOL) to fine-tune the resultant electric field pattern (Figure 1d) and fluid perfusion dynamics. The chamber pattern was cut from a 250 µm thick sheet of silicone rubber (Bisco HT-6240, Stockwell Elastomers) by a computer-controlled cutter (Cameo, Silhouette). This silicone stencil was applied to the center of a 10 cm diameter plastic tissue culture dish (Falcon). This stencil formed the watertight outline of the electro-stimulation zone against the plastic substrate. In the case of keratinocytes, fibronectin was adsorbed to the dish's surface to provide a matrix for cellular adhesion (protein dissolved to 50 µg mL^{-1} in DI water, applied to the dish for 30 min at 37 °C, then washed with DI water). To seed tissues in the stimulation zone and control the shape and size of monolayers, a second silicone stencil containing square microwells was cut and applied to the center of the culture substrate. With the stencil in place, a seeding solution of cells was prepared at a density of 2.2×10^6 cells for MDCKs and 1.7×10^6 cells for keratinocytes. 10 mL of the cell solution was pipetted into the tissue stencils at a ratio of 2 µL of solution per 5 mm^2 of stencil area. Extra humidification media was added to the periphery of the tissue culture dish and MDCK cells were allowed to settle for 1 h, whereupon sufficient media was added to fill the dish and it was left to incubate for 16 h. For keratinocytes, the cells were allowed to settle for 6 h and incubated for 14 h to account for substrate adhesion differences.

The complete device assembly consisted of four Ag/AgCl stimulation foil electrodes, four Ti wire recording electrodes,

an acrylic salt reservoir insert, and a lid cap. The three acrylic pieces comprising the reusable salt water reservoir insert were all cut from a 5.2 mm thick acrylic sheet using a computer controlled laser cutter (VLS 3.5, Universal Laser Systems). These individual layers of acrylic were stacked, clamped, then solvent welded together with acrylic cement (SCIGRIP 4, SCIGRIP Assembly Adhesives) and left to set for 72 h. The lid cap for the assembly was cut from a 3 mm thick acrylic sheet and a 1 mm-thick silicone sheet was attached to its bottom side to provide a better seal against the reservoir insert. All components were sterilized by exposure to 5 min UV radiation in a cell culture hood before assembly.

After the incubation period, the cell stencil was removed and the device was assembled within 2 h after the stencil removal. To produce the integrated salt bridges, agarose was melted into phosphate buffered saline at pH 7.4 (PBS) at 4% w/v on a hot plate. Once fully melted, the agarose was cast into the four slots in the main insert to serve as bridges. Once the agarose bridges had solidified, 3 mL of PBS was added to each of the salt reservoirs. Then, the filled and cast insert was placed over the tissue culture dish and aligned against the silicone stencil and pressed into place, taking care to avoid trapping air bubbles between the stimulation zone and the insert. Next, the four Ag/AgCl stimulation electrodes were inserted into the lid cap and the lid cap was pressed against the reservoir insert. The four recording electrodes were then pushed through the lid cap, each one making contact with one of the agarose bridges. Once everything was in place, four modified C-clamps (Humboldt Manufacturing Co.) were used to hold the assembly together. Once assembled, the device was immediately brought to the microscope for imaging.

Electrochemical system.

Electrode preparation. To produce the stimulation electrodes, 125 µm silver foil (Alfa Aesar) was cut into 1.25 cm by 5 cm strips and chloridized electrochemically; the silver working electrodes were immersed in 0.25 M KCl and subsequently connected to the positive terminal of a programmable DC power supply (Rigol DP832), and a 25 cm coiled Ti wire (0.5 mm, Alfa Aesar) was used as the counter electrode to drive 100 µA cm^{-2} plating current for 8 h. Once plated, the electrodes were washed in DI and slightly curled in preparation for assembly. Four Ti wires (0.5 mm diameter, Alfa Aesar) were cut to 5 cm length to serve as voltage recording electrodes for the closed-loop voltage controller.

Instrumentation. Two Keithley source meters (Keithley 2400/2450, Tektronix) provided current to the stimulation electrode pairs, with each meter providing one axis of stimulation. A USB oscilloscope (Analog Discovery 2, Digilent Inc.) measured the voltage across each pair of recording electrodes. A custom MATLAB script was used to command the instruments to drive a set current and measure the resultant voltage across the stimulation chamber, using proportional feedback control to adjust the output current required to maintain the target field strength and direction. Only one axis was activated at a time to maximize field uniformity within the stimulation zone. In this work, the field strength was set at ~2 V cm^{-1}. To produce intermediate stimulation directions between the horizontal and vertical axes when required, each 20 sec stimulation cycle was divided between a horizontal and vertical stimulation period (T_x and T_y, respectively) in order. The effective stimulation angle approximated by this stimulation scheme can be calculated by Equation 4:

$$\theta_{\text{eff}} = \tan^{-1}\left(\frac{T_y}{T_x}\right) \quad \textbf{(4)}$$

For example, if a 30-degree angle from the horizontal were desired, (T_x, T_y) would be set to (13 sec, 7 sec), so θ_{eff} is 28°. T_x and T_y were programmed to 1 sec resolution, meaning that 20 unique angles were possible over 90 degrees, resulting in an average field direction resolution of 4.5°. Arbitrary stimulation functions, like the 8-hour circle in Figure 5, were piecewise parameterized to produce a sequence of angles, each lasting 20 sec, that best approximated the function. In practice, the desired angle changed slowly. In the case of the circle, each angle was stimulated for an average of 3 minutes (9 stimulation cycles) before SCHEEPDOG proceeded to the next angle.

Microscopy. All images were acquired on an automated Zeiss (Observer Z1) inverted fluorescence microscope equipped with an XY motorized stage and controlled using Slidebook (Intelligent Imaging Innovations, 3i). The microscope was fully incubated at 37 °C, and a peristaltic pump (Instech Laboratories) placed within the chamber was used to continually perfuse fresh media through the electro-bioreactor at a rate of 2 mL h^{-1}. Media pH was regulated by continuously bubbling 5% CO_2 through the inlet media reservoir during perfusion. All imaging was performed using a 5X/0.16 phase-contrast objective. Nuclear labeling was performed using Hoechst 33342 (Invitrogen), a DAPI filter set (358 nm excitation, 461 nm emission), and 30 msec exposure with a metal halide lamp (xCite 120, EXFO). Images were taken at either 5 min or 10 min intervals as indicated in the text.

Image processing and analysis. All post-processing of tissue microscopy images was performed using FIJI. Images were collected sequentially, tiled, and template matched to correct for stage drift prior to being analyzed for either PIV or cellular tracking analysis.

Trajectory generation via nuclear tracking. Nuclear labeling was performed using either a custom-written machine-learning classifier trained to detect individual nuclei from phase contrast data (all MDCK data) or using Hoechst labeling (all keratinocyte data). Resulting nuclei were tracked using FIJI's TrackMate plugin set to detect spots via Laplacian of the Gaussian filtering and to link using Linear Motion Tracking (Tinevez et al., 2017). Mean population trajectories for a given maneuver were calculated by averaging the X- and Y-coordinates of all tracks at each time point.

Particle image velocimetry. Tissue migratory flow fields were generated using PIVLab, a MATLAB script performing FFT-based PIV (Thielicke and Stamhuis, 2014). PIV analysis was

performed over the central zone of the target tissue (~65% of the total area) to avoid edge artifacts as described in Cohen et al. 2014. Iterative window analysis was performed using first 96 x 96 pixel windows followed by 48 x 48 pixel windows, both with 50% step overlap. Vector validation excluded vectors beyond five standard deviations and replaced them with interpolated vectors. The velocity vector fields were then imported into MATLAB to calculate the speed and migration orientation. Rosette plots that show the direction of motion of each cell at a given time point were extracted by calculating the mean angle across the vector field.

Boundary edge displacement kymographs. Boundary images and kymographs were produced using FIJI. For the kymographs, the X-position of the tissue edge was averaged across the entire length of the tissue using a median averaging algorithm, then stacked temporally. Boundary images were produced by Gaussian blurring each frame in FIJI to create a binary binding box for the cells, then detecting the edges of each of these frames to overlay them temporally. Boundary displacement distance was calculated by measuring the distance between the maximum X-position or Y-position of the leading edge boundary both before and after stimulation.

Tissue center of mass. Cell nuclei images were median filtered to reduce background noise, then binarized using thresholding in FIJI. The binary images were them imported into MATLAB to find the tissue centroid at each frame by calculating the ensemble average of the centroids of all nuclei within the tissue.

Orientation analysis. Quantification of cell orientation was performed using FIJI's directionality analysis plugin. Fourier components analysis was used to determine a histogram for the distribution of angles present in each phase contrast image (Liu, 1991). A Gaussian function was fit to this histogram. The center of this gaussian was reported as the dominant angle. Migration angles were computed from the tracked trajectories and the mean and standard deviation of these angles were calculated by the MATLAB CircStat toolbox (Berens et al., 2009).

ACKNOWLEDGEMENTS
The primary keratinocyte line and E-media were supplied by the lab of Dr. Danelle Devenport. We thank Lena Basta for her assistance with keratinocyte cell culture. We thank Julienne LaChance for her assistance in labeling MDCK nuclei from phase contrast images via computer vision. We thank Dr. Richard Henriques for maxing the bioRχiv LaTeX template publicly available.

AUTHOR CONTRIBUTIONS
T.J.Z., G.S., A.R., and D.J.C. designed the stimulation device and experiments and T.J.Z., G.S., and L.W. performed the experiments. T.J.Z, G.S., and D.J.C. wrote the manuscript. D.J.C designed and supervised the study.

DECLARATION OF INTERESTS
The authors declare no competing interests.

References

Allen, G. M., Mogilner, A. and Theriot, J. A. (2013). Electrophoresis of cellular membrane components creates the directional cue guiding keratocyte galvanotaxis. Current Biology *23*, 560–568.

Barker, A., Jaffe, L. and Vanable Jr, J. (1982). The glabrous epidermis of cavies contains a powerful battery. American Journal of Physiology-Regulatory, Integrative and Comparative Physiology *242*, R358–R366.

Bashirzadeh, Y., Poole, J., Qian, S. and Maruthamuthu, V. (2018). Effect of pharmacological modulation of actin and myosin on collective cell electrotaxis. Bioelectromagnetics *39*, 289–298.

Berens, P. et al. (2009). CircStat: a MATLAB toolbox for circular statistics. J Stat Softw *31*, 1–21.

Berthier, E. and Beebe, D. (2014). Gradient generation platforms: new directions for an established microfluidic technology. Lab on a Chip *14*, 3241–3247.

Borgens, R. B., Vanable, J. W. and Jaffe, L. F. (1977). Bioelectricity and regeneration: large currents leave the stumps of regenerating newt limbs. Proceedings of the National Academy of Sciences *74*, 4528–4532.

Cho, Y., Son, M., Jeong, H. and Shin, J. H. (2018). Electric field–induced migration and intercellular stress alignment in a collective epithelial monolayer. Molecular biology of the cell *29*, 2292–2302.

Cohen, D. J., Nelson, W. J. and Maharbiz, M. M. (2014). Galvanotactic control of collective cell migration in epithelial monolayers. Nature materials *13*, 409.

Cole, J. and Gagnon, Z. (2019). A flow-based microfluidic device for spatially quantifying intracellular calcium ion activity during cellular electrotaxis. Biomicrofluidics *13*, 064107.

Cortese, B., Palama, I. E., D'Amone, S. and Gigli, G. (2014). Influence of electrotaxis on cell behaviour. Integrative Biology *6*, 817–830.

Dineur, E. (1891). Note sur la sensibilite des leucocytes a l'electricite. Bull Seances Soc Belge Microsc *18*, 113–118.

Du Bois-Reymond, E. (1849). Untersuchungen uber thierische Elektricitat.

Friedl, P. and Gilmour, D. (2009). Collective cell migration in morphogenesis, regeneration and cancer. Nature reviews Molecular cell biology *10*, 445.

Fuller, D., Chen, W., Adler, M., Groisman, A., Levine, H., Rappel, W.-J. and Loomis, W. F. (2010). External and internal constraints on eukaryotic chemotaxis. Proceedings of the National Academy of Sciences *107*, 9656–9659.

Gao, R., Zhao, S., Jiang, X., Sun, Y., Zhao, S., Gao, J., Borleis, J., Willard, S., Tang, M., Cai, H. et al. (2015). A large-scale screen reveals genes that mediate electrotaxis in Dictyostelium discoideum. Sci. Signal. *8*, ra50–ra50.

Hammerick, K. E., Longaker, M. T. and Prinz, F. B. (2010). In vitro effects of direct current electric fields on adipose-derived stromal cells. Biochemical and biophysical research communications *397*, 12–17.

Hou, H.-S., Tsai, H.-F., Chiu, H.-T. and Cheng, J.-Y. (2014). Simultaneous chemical and electrical stimulation on lung cancer cells using a multichannel-dual-electric-field chip. Biomicrofluidics *8*, 052007.

Huang, L. R., Tegenfeldt, J. O., Kraeft, J. J., Sturm, J. C., Austin, R. H. and Cox, E. C. (2001). Generation of large-area tunable uniform electric fields in microfluidic arrays for rapid DNA separation. In International Electron Devices Meeting. Technical Digest (Cat. No. 01CH37224) pp. 16.3.1–16.3.4, IEEE.

Huang, Y.-J., Samorajski, J., Kreimer, R. and Searson, P. C. (2013). The influence of electric field and confinement on cell motility. PloS one *8*, e59447.

Kress, H., Park, J.-G., Mejean, C. O., Forster, J. D., Park, J., Walse, S. S., Zhang, Y., Wu, D., Weiner, O. D., Fahmy, T. M. et al. (2009). Cell stimulation with optically manipulated microsources. Nature methods *6*, 905.

Lalli, M. L. and Asthagiri, A. R. (2015). Collective migration exhibits greater sensitivity but slower dynamics of alignment to applied electric fields. Cellular and molecular bioengineering *8*, 247–257.

Li, J. and Lin, F. (2011). Microfluidic devices for studying chemotaxis and electrotaxis. Trends in cell biology *21*, 489–497.

Li, L., Hartley, R., Reiss, B., Sun, Y., Pu, J., Wu, D., Lin, F., Hoang, T., Yamada, S., Jiang, J. et al. (2012). E-cadherin plays an essential role in collective directional migration of large epithelial sheets. Cellular and Molecular Life Sciences *69*, 2779–2789.

Liu, Z.-Q. (1991). Scale space approach to directional analysis of images. Applied optics *30*, 1369–1373.

McCaig, C. D., Song, B. and Rajnicek, A. M. (2009). Electrical dimensions in cell science. Journal of cell science *122*, 4267–4276.

Meng, X., Arocena, M., Penninger, J., Gage, F. H., Zhao, M. and Song, B. (2011). PI3K mediated electrotaxis of embryonic and adult neural progenitor cells in the presence of growth factors. Experimental neurology *227*, 210–217.

Nuccitelli, R. (2003). A role for endogenous electric fields in wound healing. Current topics in developmental biology *58*, 1–26.

Poujade, M., Grasland-Mongrain, E., Hertzog, A., Jouanneau, J., Chavrier, P., Ladoux, B., Buguin, A. and Silberzan, P. (2007). Collective migration of an epithelial monolayer in response to a model wound. Proceedings of the National Academy of Sciences *104*, 15988–15993.

Sarkar, A., Kobylkevich, B. M., Graham, D. M. and Messerli, M. A. (2019). Electromigration of cell surface macromolecules in DC electric fields during cell polarization and galvanotaxis. Journal of theoretical biology *478*, 58—73.

Schopf, A., Boehler, C. and Asplund, M. (2016). Analytical methods to determine electrochemical factors in electrotaxis setups and their implications for experimental design. Bioelectrochemistry *109*, 41–48.

Shellard, A., Szabó, A., Trepat, X. and Mayor, R. (2018). Supracellular contraction at the rear of neural crest cell groups drives collective chemotaxis. Science *362*, 339–343.

Shrestha, R., Little, K. A., Tamayo, J. V., Li, W., Perlman, D. H. and Devenport, D. (2015). Mitotic control of planar cell polarity by polo-like kinase 1. Developmental cell *33*, 522–534.

Song, B., Gu, Y., Pu, J., Reid, B., Zhao, Z. and Zhao, M. (2007). Application of direct current electric fields to cells and tissues in vitro and modulation of wound electric field in vivo. Nature protocols *2*, 1479.

Song, S., Han, H., Ko, U. H., Kim, J. and Shin, J. H. (2013). Collaborative effects of electric field and fluid shear stress on fibroblast migration. Lab on a Chip *13*, 1602–1611.

Sroka, J., Zimolag, E., Lasota, S., Korohoda, W. and Madeja, Z. (2018). Electrotaxis: Cell Directional Movement in Electric Fields pp. 325–340. Springer.

Sun, Y.-S. (2017). Studying electrotaxis in microfluidic devices. Sensors , *17*, 2048.

Tai, G., Reid, B., Cao, L. and Zhao, M. (2009). Electrotaxis and wound healing: experimental methods to study electric fields as a directional signal for cell migration. In Chemotaxis, pp. 77–97. Springer.

Tandon, N., Cannizzaro, C., Chao, P.-H. G., Maidhof, R., Marsano, A., Au, H. T. H., Radisic, M. and Vunjak-Novakovic, G. (2009). Electrical stimulation systems for cardiac tissue engineering. Nature protocols , *4*, 155.

Thielicke, W. and Stamhuis, E. (2014). PIVlab–towards user-friendly, affordable and accurate digital particle image velocimetry in MATLAB. Journal of Open Research Software , *2*.

Tinevez, J.-Y., Perry, N., Schindelin, J., Hoopes, G. M., Reynolds, G. D., Laplantine, E., Bednarek, S. Y., Shorte, S. L. and Eliceiri, K. W. (2017). TrackMate: An open and extensible platform for single-particle tracking. Methods , *115*, 80–90.

Toettcher, J. E., Weiner, O. D. and Lim, W. A. (2013). Using optogenetics to interrogate the dynamic control of signal transmission by the Ras/Erk module. Cell , *155*, 1422–1434.

Trepat, X., Wasserman, M. R., Angelini, T. E., Millet, E., Weitz, D. A., Butler, J. P. and Fredberg, J. J. (2009). Physical forces during collective cell migration. Nature physics , *5*, 426.

Tsai, H.-F., Cheng, J.-Y., Chang, H.-F., Yamamoto, T. and Shen, A. Q. (2016). Uniform electric field generation in circular multi-well culture plates using polymeric inserts. Scientific reports , *6*, 26222.

Vulto, P., Huesgen, T., Albrecht, B. and Urban, G. (2009). A full-wafer fabrication process for glass microfluidic chips with integrated electroplated electrodes by direct bonding of dry film resist. Journal of Micromechanics and Microengineering , *19*, 077001.

Wu, S.-Y., Hou, H.-S., Sun, Y.-S., Cheng, J.-Y. and Lo, K.-Y. (2015). Correlation between cell migration and reactive oxygen species under electric field stimulation. Biomicrofluidics , *9*, 054120.

Xiong, S., Gao, H., Qin, L., Jia, Y.-G. and Ren, L. (2019). Engineering topography: Effects on corneal cell behavior and integration into corneal tissue engineering. Bioactive Materials , *4*, 293–302.

Zhao, M., Bai, H., Wang, E., Forrester, J. V. and McCaig, C. D. (2004). Electrical stimulation directly induces pre-angiogenic responses in vascular endothelial cells by signaling through VEGF receptors. Journal of cell science , *117*, 397–405.

Zhao, M., Song, B., Pu, J., Wada, T., Reid, B., Tai, G., Wang, F., Guo, A., Walczysko, P., Gu, Y. et al. (2006). Electrical signals control wound healing through phosphatidylinositol-3-OH kinase-γ and PTEN. Nature , *442*, 457.

Supplemental Information

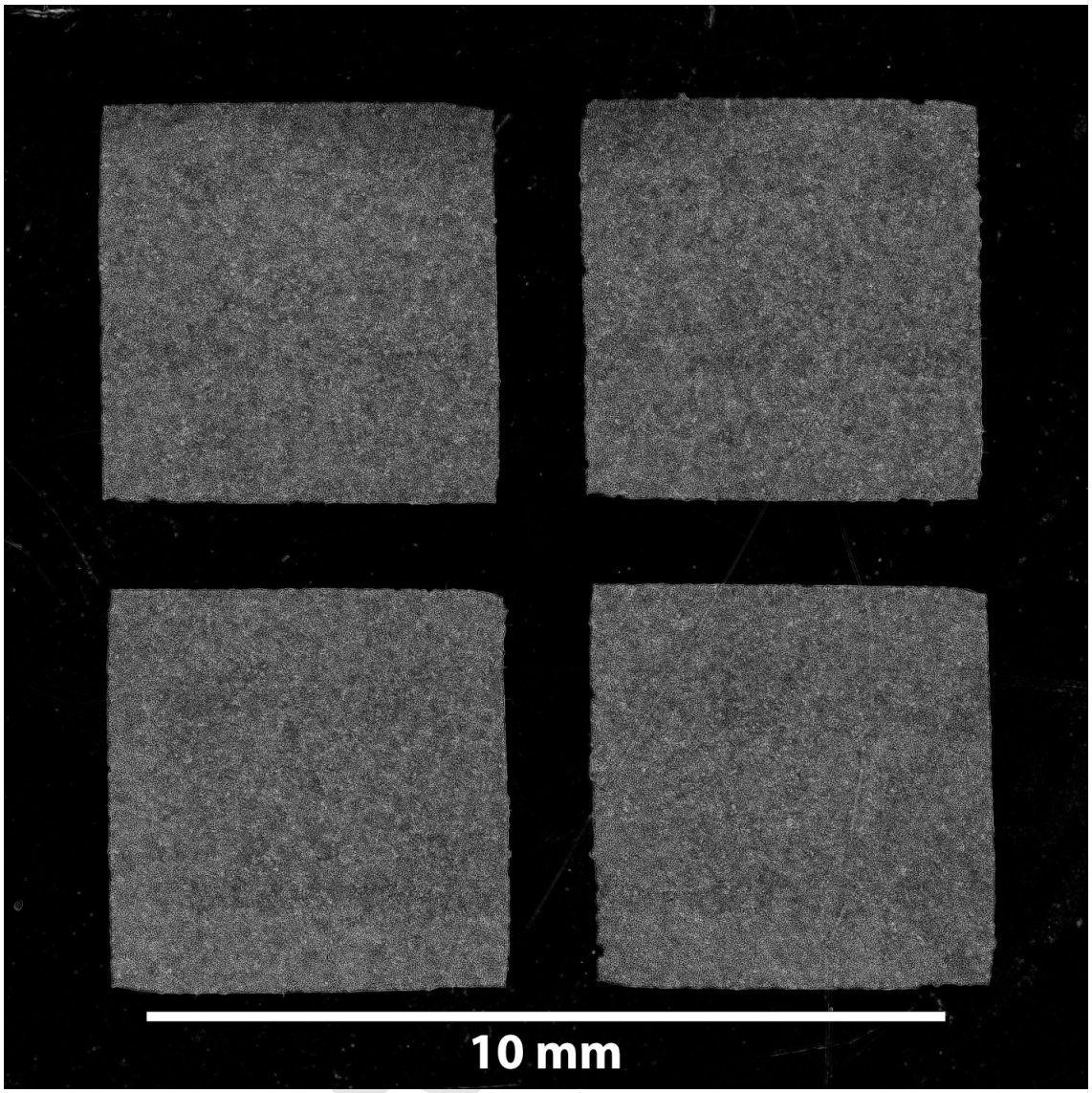

Figure S1. Phase-contrast microscopy image of four 5x5 mm MDCK monolayers patterned inside the SCHEEPDOG device's stimulation zone. Related to Figures 1,2. Image was background subtracted and its brightness was increased for visual clarity.

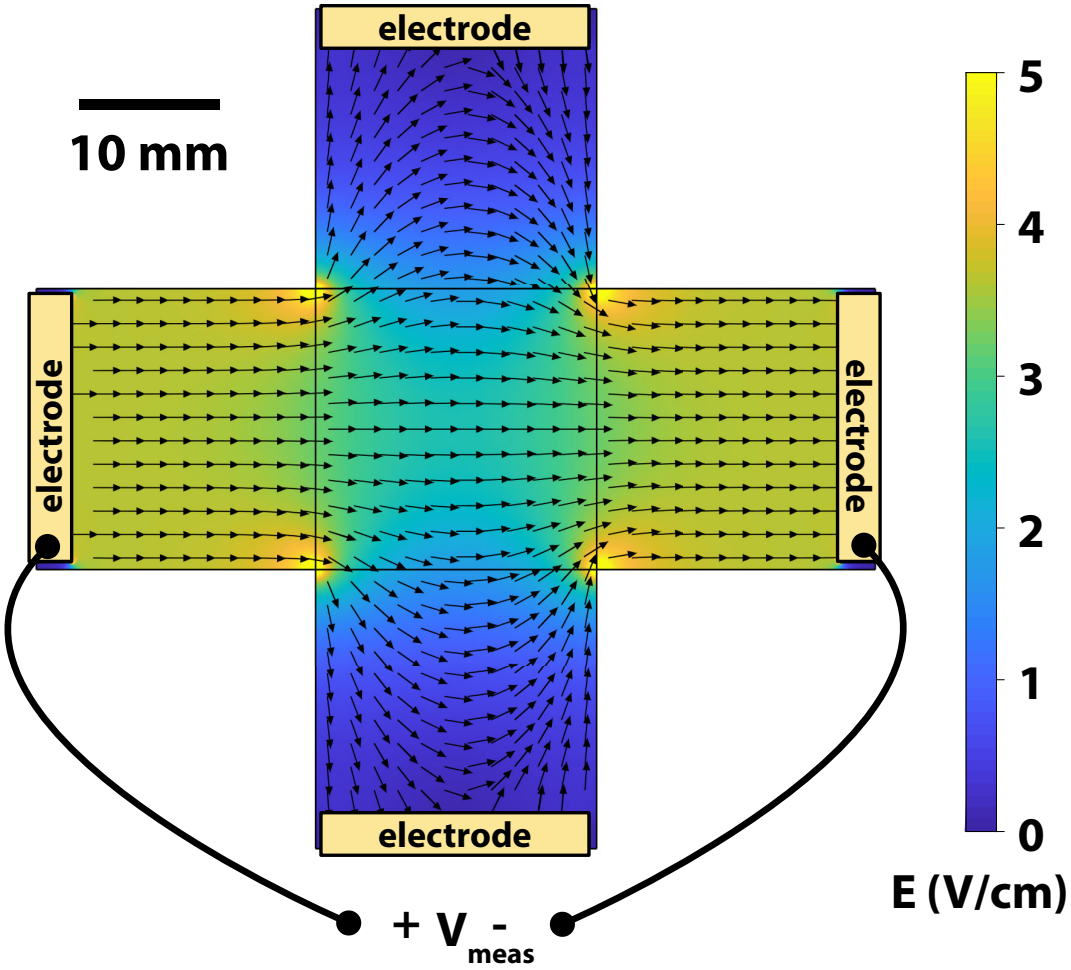

Figure S2. Naive double-axis chamber design that results in nonuniform field. Related to Figure 1. Care must be taken when adding a second pair of electrodes to an electrochemical stimulation system to avoid excessive current leak through the orthogonal axis. Otherwise, field uniformity in the center is adversely affected.

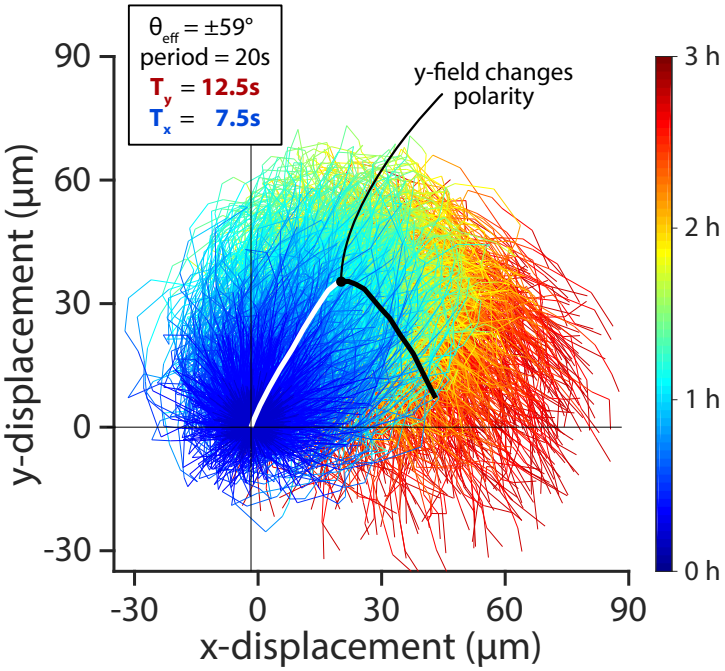

Figure S3. Trajectories from programmed 60°, then −60° diagonals in MDCK monolayer (trajectories measured from n = 2 tissues). Related to Figure 4. Mean trajectory of individual cell trajectories (white/black). Individual trajectories were taken from 2x2 mm central segments of 5x5 mm tissues during induced migration. For visual clarity, tracks within one standard deviation of the mean cell trajectory are selected and plotted as time-coded multicolor lines (n = 1337 trajectories selected from 2000). See also Movie S6.

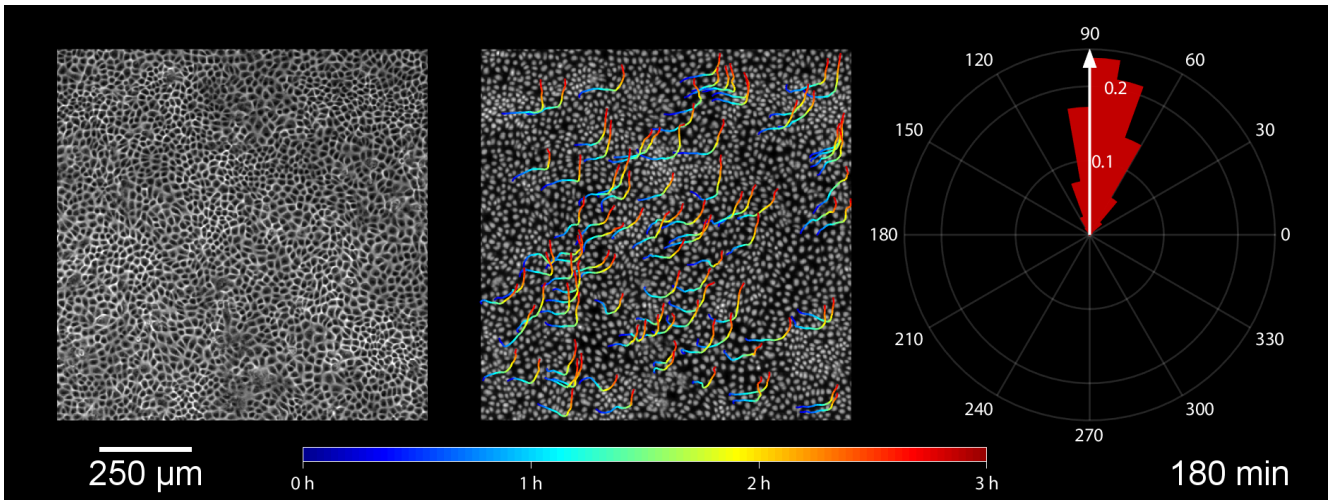

Movie S1. Timelapse of programmed 90° turn in MDCK monolayer. Field was directed for 1.5 h 'right,' then 1.5 h 'up'. Left panel shows phase-contrast microscopy of 1x1 mm section in the center of the monolayer. Center panel shows selected trajectories overlaid onto nuclear data labeled by a machine-learning classifier. Right panel shows the field direction (white arrow) overlaid onto a polar histogram of cell displacement angle at each time point. See also Figure 3.

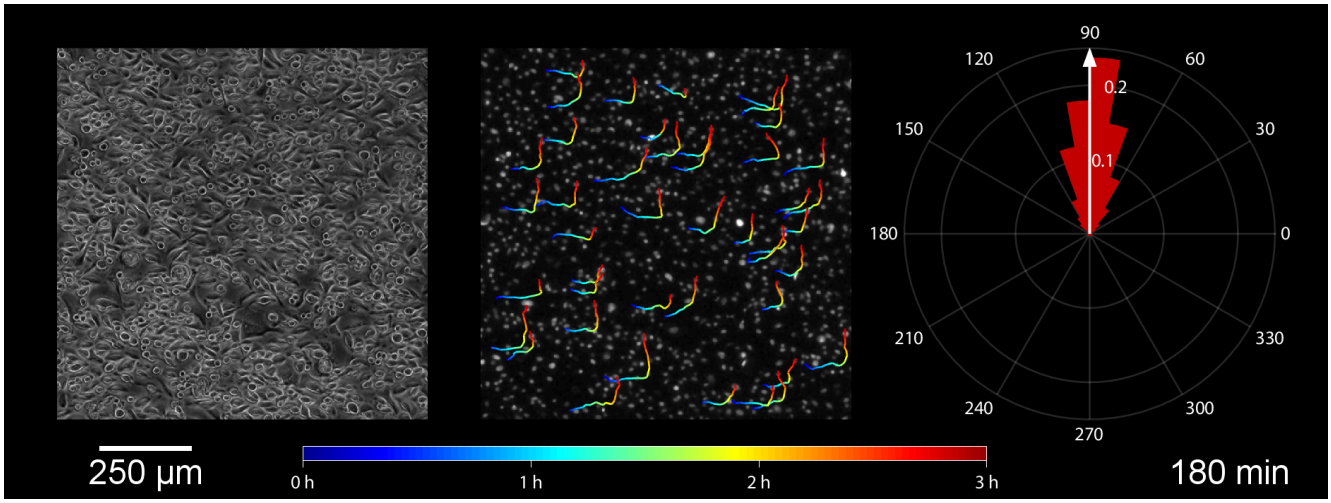

Movie S2. Timelapse of programmed 90° turn in keratinocyte monolayer. Field was directed for 1.5 h 'right,' then 1.5 h 'up'. Left panel shows phase-contrast microscopy of 1x1 mm section in the center of the monolayer. Center panel shows selected trajectories overlaid onto nuclear data collected by Hoechst 33342 labeling and fluorescence microscopy. Right panel shows the field direction (white arrow) overlaid onto a polar histogram of cell displacement angle at each time point. See also Figure 3.

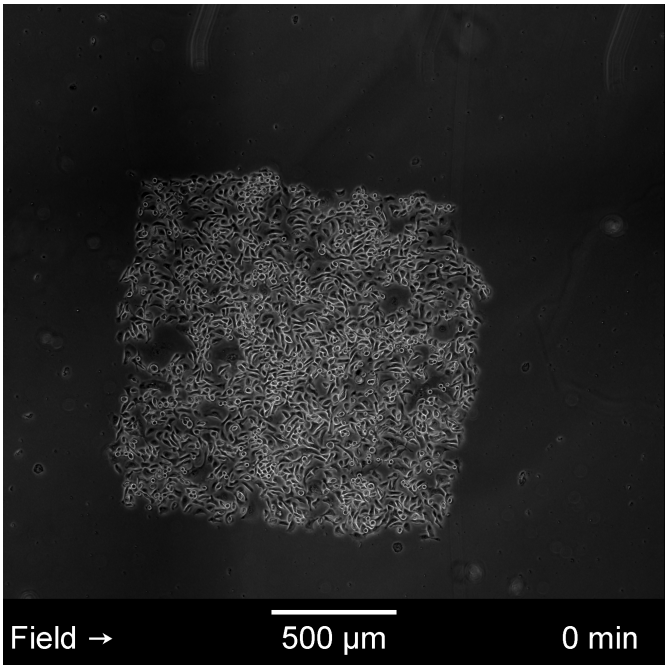

Movie S3. Timelapse of extended 90° turn in keratinocyte monolayer, showing whole tissue translation. Field was directed for 4 h 'right,' then 4 h 'up'. See also Figure 3.

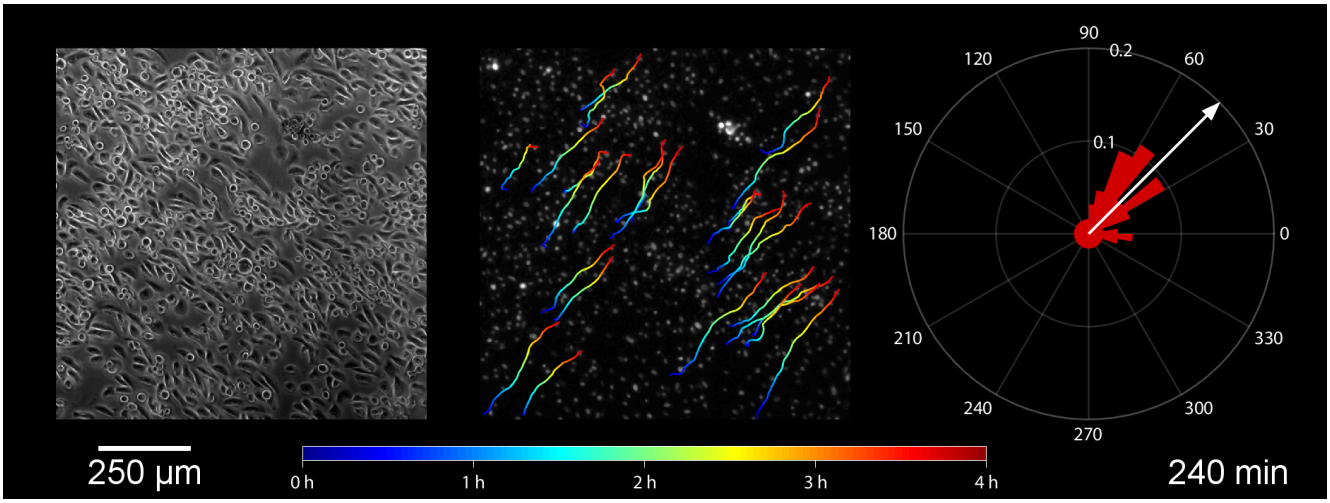

Movie S4. Timelapse of programmed 45° diagonal in keratinocyte monolayer. Field was rapidly alternated between axes for effective stimulation angle of $\theta_{\mathrm{eff}} = 45°$ for 4 h. Left panel shows phase-contrast microscopy of 1x1 mm section in the center of the monolayer. Center panel shows selected trajectories overlaid onto nuclear data collected by Hoechst 33342 labeling and fluorescence microscopy. Right panel shows the field direction (white arrow) overlaid onto a polar histogram of cell displacement angle at each time point. See also Figure 4.

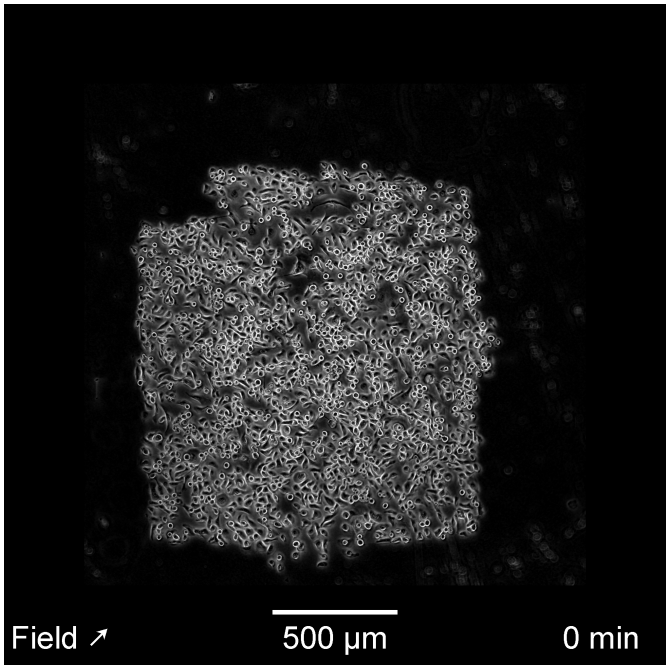

Movie S5. Timelapse of whole tissue translation at 45° angle in keratinocyte monolayer. Field was rapidly alternated between axes for effective stimulation angle of $\theta_{\mathrm{eff}} = 45°$ for 4 h. See also Figure 4.

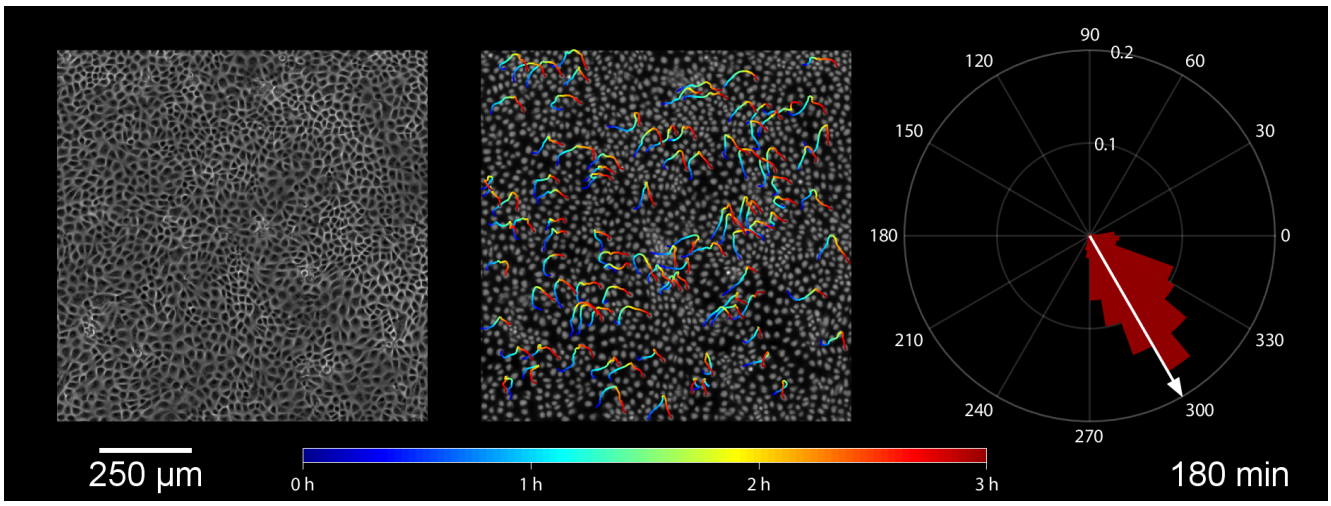

Movie S6. Timelapse of programmed 60°, then –60° diagonals in MDCK monolayer. Field was rapidly alternated between axes for effective stimulation angle of $\theta_{\mathrm{eff}} = 60°$ for 1.5 h, then $\theta_{\mathrm{eff}} = -60°$ for 1.5 h. Left panel shows phase-contrast microscopy of 1x1 mm section in the center of the monolayer. Center panel shows selected trajectories overlaid onto nuclear data labeled by a machine-learning classifier. Right panel shows the field direction (white arrow) overlaid onto a polar histogram of cell displacement angle at each time point. See also Figure S3.

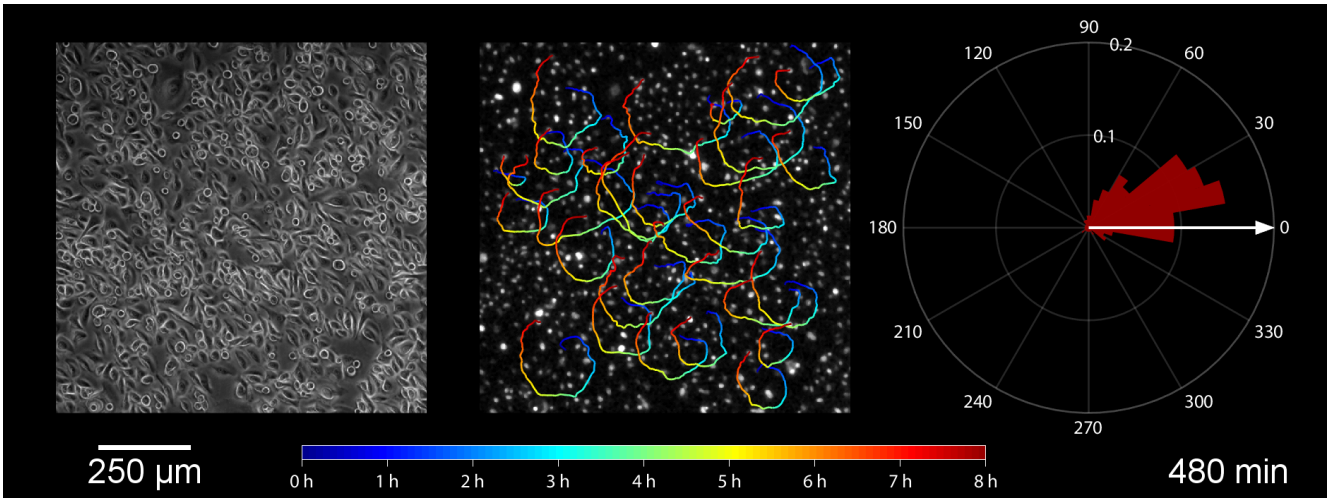

Movie S7. Timelapse of programmed circle maneuver in keratinocyte monolayer. Field was rapidly alternated between axes to rotate the field clockwise at a rate of 45 $°h^{-1}$ over 8 h. Left panel shows phase-contrast microscopy of 1x1 mm section in the center of the monolayer. Center panel shows selected trajectories overlaid onto nuclear data collected by Hoechst 33342 labeling and fluorescence microscopy. Right panel shows the field direction (white arrow) overlaid onto a polar histogram of cell displacement angle at each time point. See also Figure 5.